



UNIVERSITY OF LEEDS

This is a repository copy of *Pyrite oxidation in shales: Implications for palaeo-redox proxies based on geochemical and SEM-EDX evidence*.

White Rose Research Online URL for this paper:

<http://eprints.whiterose.ac.uk/147852/>

Version: Accepted Version

---

**Article:**

Mahoney, C, März, C orcid.org/0000-0003-2558-4711, Buckman, J et al. (2 more authors) (2019) Pyrite oxidation in shales: Implications for palaeo-redox proxies based on geochemical and SEM-EDX evidence. *Sedimentary Geology*, 389. pp. 186-199. ISSN 0037-0738

<https://doi.org/10.1016/j.sedgeo.2019.06.006>

---

© 2019 Elsevier B.V. All rights reserved. Licensed under the Creative Commons Attribution-Non Commercial No Derivatives 4.0 International License (<https://creativecommons.org/licenses/by-nc-nd/4.0/>).

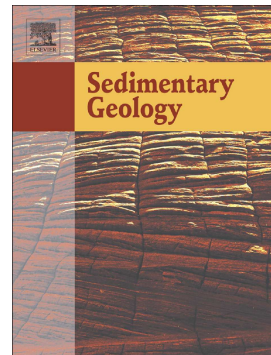
**Reuse**

This article is distributed under the terms of the Creative Commons Attribution-NonCommercial-NoDerivs (CC BY-NC-ND) licence. This licence only allows you to download this work and share it with others as long as you credit the authors, but you can't change the article in any way or use it commercially. More information and the full terms of the licence here: <https://creativecommons.org/licenses/>

**Takedown**

If you consider content in White Rose Research Online to be in breach of UK law, please notify us by emailing [eprints@whiterose.ac.uk](mailto:eprints@whiterose.ac.uk) including the URL of the record and the reason for the withdrawal request.

# Accepted Manuscript



Pyrite oxidation in shales: Implications for palaeo-redox proxies based on geochemical and SEM-EDX evidence

Carol Mahoney, Christian März, Jim Buckman, Tom Wagner,  
Vladimir-Orlando Blanco-Velandia

PII: S0037-0738(19)30138-1

DOI: <https://doi.org/10.1016/j.sedgeo.2019.06.006>

Reference: SEDGEO 5505

To appear in: *Sedimentary Geology*

Received date: 8 March 2019

Revised date: 12 June 2019

Accepted date: 15 June 2019

Please cite this article as: C. Mahoney, C. März, J. Buckman, et al., Pyrite oxidation in shales: Implications for palaeo-redox proxies based on geochemical and SEM-EDX evidence, *Sedimentary Geology*, <https://doi.org/10.1016/j.sedgeo.2019.06.006>

This is a PDF file of an unedited manuscript that has been accepted for publication. As a service to our customers we are providing this early version of the manuscript. The manuscript will undergo copyediting, typesetting, and review of the resulting proof before it is published in its final form. Please note that during the production process errors may be discovered which could affect the content, and all legal disclaimers that apply to the journal pertain.

# Pyrite oxidation in shales: Implications for palaeo-redox proxies based on geochemical and SEM-EDX evidence

Carol Mahoney<sup>a</sup>, Christian März<sup>a</sup>, Jim Buckman<sup>b</sup>, Tom Wagner<sup>c</sup>, Vladimir-Orlando Blanco-Velandia<sup>d</sup>

<sup>a</sup>School of Earth and Environment, Leeds University, LS2 9JT, United Kingdom.

<sup>b</sup>Institute of Petroleum Engineering, Heriot-Watt University, Edinburgh, EH14 4AS, United Kingdom

<sup>c</sup>The Lyell Centre, Heriot-Watt University, Research Avenue South, Edinburgh, EH14 4AP, United Kingdom

<sup>d</sup>Instituto Colombiano del Petróleo, Ecopetrol, Bucaramanga, Colombia

Corresponding author: Carol Mahoney ([c.mahoney@leeds.ac.uk](mailto:c.mahoney@leeds.ac.uk))

## Abstract

Pyrite oxidation in marine shales during weathering has been widely studied, however, the effects of this process on geochemical proxies commonly used to reconstruct ocean redox conditions, or the details of pyrite oxidation at the mineral grain scale, have not received much scientific attention. We conducted a four-week laboratory experiment designed to stimulate pyrite oxidation at shale outcrops, and to assess effects on the chemical phase of iron and sulphur in the samples both in bulk sediments (useful for comparison to palaeo-environmental geochemistry) and at a finer scale (to gain a better understanding of the nature of these changes). Geochemical and scanning electron microscopy (SEM) techniques provide evidence for pyrite oxidation, carbonate dissolution, and iron (oxyhydr)oxide

formation during the experiment. The net effect of the experiment on the ratio of highly reactive iron phases ( $\text{Fe}_{\text{HR}}$ ) to total iron ( $\text{Fe}_{\text{T}}$ ) is minimal (<0.03% difference), suggesting that this redox proxy behaves relatively conservatively during weathering. The effect of weathering on the ratio of pyrite-bound iron to highly reactive iron ( $\text{Fe}_{\text{PY}}/\text{Fe}_{\text{HR}}$ ), used to investigate the availability of sulphur, in contrast, is pronounced (up to 32.5% difference) due to the oxidation of pyrite and the precipitation of iron (oxyhydr)oxides in the shale samples. Electron microscopy provides evidence that iron (oxyhydr)oxides precipitated *in situ* as rims around cores of pyrite particles, “passivating” and protecting them from further oxidation. The quantification of these partly oxidised pyrite particles is now possible using a novel automated particle analysis method coupled to chemical mapping, developed in this study. We conclude that this method can be of wide use, both to quantify pyrite oxidation, and assess the significance of  $\text{Fe}_{\text{PY}}/\text{Fe}_{\text{HR}}$  measured in shale outcrop samples.

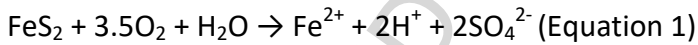
**Keywords:** weathering, pyrite, geochemistry, shale, mudrock, Fe-Speciation

## 1. Introduction

Black shales are organic-rich mudrocks that not only represent sources of fossil fuels but also serve as important palaeoenvironmental archives (Brumsack, 2006; Negri et al., 2006). Understanding the lateral and temporal dynamics of shale deposition often requires a combination of drill core and outcrop material, the latter potentially having experienced variable degrees of chemical modification due to outcrop weathering processes. The leaching of elements from shale by weathering is well documented and known to be an important process mobilising nutrients and other critical elements from the bedrock to soils, rivers and eventually the ocean (Pye and Miller, 1990; Zhu et al. 2008; Tuttle and Breit,

2009; Marthur et al., 2012; Zhu and Wu, 2012; Perkins and Mason, 2015). However, the selective loss of elements from weathered shale and the related alteration of its geochemical inventory create challenges for the interpretation of palaeoenvironmental conditions based on geochemical proxies determined from shale samples. In this study we focus on iron compounds as a well-established proxy for reconstructing water column redox conditions and sulphate availability in the depositional environment (Berner and Raiswell, 1984; Raiswell et al., 1988; Poulton and Canfield, 2011; Raiswell and Canfield, 2012), and its modification by weathering.

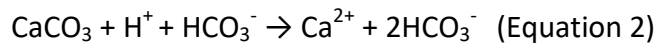
Different iron (Fe) minerals, while being important proxies for palaeo-redox conditions, are also important to the process of weathering itself. The oxidation of pyrite ( $\text{FeS}_2$ ), the dominant Fe sulphide in rocks, is key to the chemical weathering behaviour of shale. The net chemical reaction of pyrite oxidation in an aqueous solution is:



Although this is the net reaction, it is complicated by intermediary reactions which can involve different species of Fe and sulphur (S) (Chandra and Gerson, 2010). Ferrous iron produced in Eq. 1 either remains in solution or precipitates as Fe (oxyhydr)oxides or Fe sulphates like jarosite, depending on the chemical environment. As evident from Eq. 1, pyrite oxidation provides protons, which are then available for the hydrolysis of aluminosilicates and the dissolution of carbonates (Pye and Miller, 1990). The reaction also consumes oxygen, thereby inhibiting organic matter oxidation (Petsch et al., 2000; Tuttle and Breit, 2009). Understanding the processes which control the rate and mechanism of pyrite oxidation is, therefore, vital for understanding the degree of geochemical overprint imposed by shale weathering at an outcrop.

Studies on Fe compounds changes during weathering in shale are mostly limited to changes in pyrite contents (Littke et al., 1991; Petsch et al., 2000; Wildman et al., 2004; Zhu et al., 2008; Jin et al., 2013; Liao et al., 2014). Iron mineral transformations due to weathering have been studied in naturally weathered rocks using X-ray diffraction (XRD) (Pye and Miller, 1990; Tuttle and Breit, 2009) and Mössbauer spectroscopy (Odin et al., 2015a, 2015b). To our knowledge, no experiment has yet examined changes in Fe mineralogy during organic-rich mudstone weathering using the wet chemical extraction method developed by Poulton and Canfield (2005). Taking advantage of this sequential extraction method (developed from earlier methods of Raiswell et al., 1988, 1994; Poulton et al., 2004), quantitative information on the different Fe compounds present in a sedimentary rock based on their reactivity with free hydrogen sulphide ( $H_2S$ ) can be derived. In this scheme, all sedimentary Fe that has already reacted with  $H_2S$  (mainly pyrite,  $Fe_{PY}$ ) or can react with  $H_2S$  over short timescales (days to years; mainly Fe carbonates and (oxyhydr)oxides, including magnetite) are collectively summarised as the highly reactive Fe fraction ( $Fe_{HR}$ ). In combination with the analysis of total Fe ( $Fe_T$ ) in a sample, empirically tested ratios can be calculated that allow a differentiation of redox conditions in the seawater and porewater during the time of deposition. The  $Fe_{HR}/Fe_T$  ratio has been proposed as proxy to differentiate between oxic and anoxic (no free oxygen) conditions during deposition, while the  $Fe_{PY}/Fe_{HR}$  ratio allows to differentiate between anoxic, non-sulphidic (or ferruginous) and anoxic, sulphidic (or euxinic) conditions (e.g., Raiswell et al., 1988; Poulton and Canfield, 2005; Poulton and Canfield, 2011; Poulton et al., 2015). Since the  $Fe_{HR}$  fraction includes both pyrite and common products of pyrite oxidation (mainly Fe (oxyhydr)oxides), it is expected that the  $Fe_{HR}/Fe_T$  redox proxy will be less affected by outcrop weathering than the  $Fe_{PY}/Fe_{HR}$  ratio.

Dissolution of carbonate minerals (mainly calcite,  $\text{CaCO}_3$ ) is considered a key reaction in response to proton release by pyrite oxidation:



This reaction increases the porosity of the mudrock and allows oxygen and water to penetrate further into its fabric (Pye and Miller, 1990; Brantley and White, 2009; Jin et al., 2013). In the field, carbonate and pyrite weathering fronts can coincide (e.g. Brantley et al., 2017), suggesting close pyrite oxidation-carbonate dissolution relationships in shale.

Besides the chemical quantification of Fe phases using sequential or total wet chemical extraction techniques, there has been increasing interest in the applications of scanning electron microscopy (SEM) for the analysis of shales and mudrocks (Camp et al., 2013). Automated heavy mineral particle analysis in SEM allows for the rapid assessment of the morphology and chemical composition (via energy-dispersive x-ray analysis, EDX) of all dense particles (including pyrite), and for a quantitative analysis of Fe-containing minerals. Buckman et al. (2018) used automated particle analysis data from SEM-EDX to show how quantitative data can be gathered about the location of partially oxidised pyrite particles.

In this study, we present the findings of a laboratory experiment designed to stimulate pyrite oxidation within two Mesozoic black shale samples. We measured the bulk geochemistry, Fe mineralogy, and inorganic and organic carbon (TIC and TOC) in the original and treated shale samples. By comparing pyrite oxidation in the two geochemically different samples we demonstrate how the initial shale composition affects the extent, nature and further geochemical effects of pyrite oxidation. Our study differs from most laboratory weathering studies (e.g., Senkayi et al., 1981; Pye and Miller, 1990; Jeng, 1992; Schillawaski,

2008; Jin et al., 2013; Odin et al., 2015b) as it focuses on changes to Fe phase, and thus provides novel insights into the preservation or overprint of this proxy at outcrop level.

## 2. Materials

One bulk sample was taken from two different shale localities for the experiment: the Blackstone band (BSB) of the Jurassic Kimmeridge Clay Formation collected at Clavell's Hard, Kimmeridge, Dorset (e.g., Washburn and Birdwell, 2013; Armstrong et al., 2016; Bolin et al., 2016); and a Late Cretaceous shale of the Chipaque Formation taken from Quebrada Vara Santa (QVS) in the Eastern Cordillera of Colombia. Both bulk samples were collected from outcrops and therefore have already been exposed to weathering, but were collected from outcrop types commonly chosen for geochemical studies, i.e. from a quickly eroding cliff face (BSB) and a mountainous river bed (QVS). Neither showed any visible sign of chemical weathering (discolouration or surface salts), and they were collected as one large, solid sample, which had not lost physical integrity because of weathering.

Both samples differ markedly in their geochemistry. BSB is a mudstone dominated by TOC (~50 wt%; Raiswell et al., 2001; Tribouillard et al., 2004) and carbonate (35 %, this study). QVS is dominated by siliciclastic detrital material (Blanco, 2012) and has lower carbonate (3.1 %, this study) and TOC contents (2.6 %, this study), representing a mudstone with a carbonate content close to average shale (3.9 % CaCO<sub>3</sub>, Wedepohl, 1971, 1991). Both samples, however, contain similar amounts of pyrite (QVS 2.2 %, BSB 1.7 %).

### 3. Experimental setup

To stimulate pyrite oxidation in the selected shale samples, a soxhlet extractor was modified to continually drip distilled water over the shale chips contained within a cellulose thimble, before being collected in a flask, in a setup suggested by Pedro et al. (1961) (Fig. 1). The condenser was left open, allowing exchange with the atmosphere; no attempt was made to control/monitor oxygen and carbon dioxide ( $O_2$  and  $CO_2$ ) concentrations. In order to remove any areas of potentially chemically altered sample, the external faces of the two solid, bulk samples were removed. The innermost section of each bulk sample was further disaggregated with a rock hammer. These chips were sieved to 2-6mm in diameter and immediately freeze dried to remove water and minimise further weathering reactions. This process generated dry, relatively homogenous, bulk samples of QVS and BSB rock chips. The experiment was repeated four times, once with a subsample of the prepared BSB rock chips, and with three identical experiments running concurrently with subsamples of the QVS rock chips, in order to test the reproducibility of the experiment.

In each experiment, a subsample of 35-40 g of the bulk prepared chipped samples was added to a cellulose thimble in the sample container. Distilled water was added to the round bottom flask and heat was applied to generate water vapour which, when reaching the condenser, dripped onto the sample (3-6 drops/minute). The recirculating water (hereafter called effluent) was monitored and replaced periodically with distilled water. The periods between this replacement and the volume of effluent were adjusted to attempt to minimise mineral precipitation within the effluent, however, a white precipitate did form occasionally. Prior to each effluent replacement, the pH was measured using a pHenomenal

pH1000L meter (Fig. 2a), and samples of the effluent were taken. At the same time the effluent was changed, the temperature within the cellulose thimble was recorded. The temperature varied with room temperature from 33-58°C (Fig. 2b). A subsample of each effluent was treated with 20 % v/v nitric acid to adjust pH to <2 and stored at 5 °C for further analysis. Eighteen effluent samples were taken during the BSB experiment and 11 effluent samples were taken from each of the three QVS experiments.

At the end of the four-week experiment, the rock chips were removed from the thimble, freeze-dried to halt further weathering reactions, and the majority was ground in an agate ball mill for geochemical analysis. Untreated subsamples of the original freeze dried shale chips were also ground in an agate ball mill. In total, two untreated subsamples of the original homogeneous bulk, chipped sample (hereafter named QVS.1 and BSB.1) and four treated subsamples of the bulk, chipped sample (hereafter named BSB.2, and QVS.2a, QVS.2b and QVS.2c) were ground and analysed. A subsample of untreated chips from the bulk samples and treated chips was prepared for analysis by SEM.

#### 4. Methods

##### 4.1 Bulk sample analysis

The bulk geochemistry (measured elements listed in Table 1) of the original and treated samples was determined using wavelength-dispersive X-ray fluorescence (XRF) (Axios Plus XRF, PANalytical). A subsample of around 0.7 g was mixed with 2 g of di-lithium tetraborate ( $\text{Li}_2\text{B}_4\text{O}_{10}$ ) and pre-oxidised overnight with 1 g ammonium nitrate ( $\text{NH}_4\text{NO}_3$ ) for preoxidation of organic matter and sulphides prior to fusion to produce a glass bead (Eckert et al., 2013). Samples were measured alongside an in-house standard with a precision of RSD <5 % for all elements reported.

One hundred mg of each bulk ground sample was weighed into a ceramic vessel for total carbon (TC) determination by a Leco CS230 Carbon-Sulphur analyser. Total organic carbon was determined by the same method on a second subsample after the removal of carbonates by hot hydrochloric acid. Total inorganic carbon (TIC) was calculated as the difference between TC and TOC. Total inorganic carbon is likely to reside in calcium carbonate (calcite), with minor contributions of dolomite (magnesium calcite) and Fe-associated carbonates. Triplicate analysis showed an average precision of 5.1 % relative standard deviation (RSD) for the LECO analysis. Fifty mg of powdered sample were accurately weighed into clean ceramic crucibles and analysed for their S contents using an Elementar Vario Max CNS Macro Elemental Analyzer, alongside sulfadiazine as a calibration standard. Repeat measurements (triplicate on two samples) showed an average precision of <5 % RSD for TC and TOC. Duplicate measurements on four samples show a precision of <1% RSD for S.

The nature of the Fe compounds was determined using a sequential extraction method developed by Poulton and Canfield (2005). This procedure involves exposing samples to progressively stronger reagents to extract Fe from progressively less reactive Fe compound pools (Table 1). Four Fe pools were extracted,  $\text{Fe}_{\text{carb}}$  (carbonate-associated Fe including siderite and ankerite),  $\text{Fe}_{\text{ox1}}$  (amorphous and poorly crystalline (oxyhydr)oxides, e.g. ferrihydrite and lepidocrocite),  $\text{Fe}_{\text{ox2}}$  (crystalline oxides, e.g. goethite, akaganéite and hematite) and  $\text{Fe}_{\text{mag}}$  (magnetite). The resultant extraction solutions were analysed for Fe concentrations using atomic absorption spectroscopy (AAS). From separate subsamples from the bulk ground samples, pyrite was extracted using the stoichiometric technique prescribed by Canfield et al. (1986), whereby metal sulphides (predominately pyrite) are reduced using a boiling chromous chloride ( $\text{Cr(II)Cl}_2$ ) solution. Triplicate measurements (four samples for the sequential extraction and three samples for the pyrite extraction) indicated an average precision of 7 % RSD in the sequential extraction and 2 % RSD in the pyrite extraction. Poorly reactive Fe ( $\text{Fe}_{\text{PRS}}$ ) was defined as the difference between total Fe and the sum of the five extracted Fe species (Fe in pyrite ( $\text{Fe}_{\text{PY}}$ ),  $\text{Fe}_{\text{carb}}$ ,  $\text{Fe}_{\text{ox1}}$ ,  $\text{Fe}_{\text{ox2}}$ ,  $\text{Fe}_{\text{mag}}$ ).

#### 4.2 Effluent analysis

Acidified effluent samples were analysed using inductively coupled plasma optical emission spectroscopy (ICP-OES) (Varian Vista-MPX). A multi-element standard was used to correct for instrument deviation every 10 samples and Scandium was used as an internal recovery standard at 5 ppm. Each sample was measured three times with an RSD of <5.5 % for major elements.

#### 4.3 SEM-EDX analysis

After vacuum impregnation with resin, rock chips before and after the experiment were made into polished thin sections. They were then analysed, uncoated, using SEM (Quanta 650 field-emission SEM) operated in low-vacuum mode. Images were collected with a standard quad back-scattered electron (BSE) detector at 20kV, with a spot size of 4.5. In addition, an EDX detector (Oxford Instruments X-Max<sup>N</sup> 150 mm) was used to scan across the sample using the particle analysis software AZtecFeature to detect heavy mineral particles. A series of fields of view were scanned, with a dwell time of 35 microseconds, having a horizontal field of view of 259 microns and 1024 pixels. Each image was thresholded and all bright particles were automatically selected for analysis by EDX. The whole area of each feature was scanned, using a process time of 1 and an acquisition time of 0.50 live seconds. Particles smaller than 0.49 microns equivalent circular diameter (ECD), equating to 3 pixels, were automatically filtered out. Each particle was analysed in terms of its elemental composition and a range of physical parameters, which included X-Y location coordinates.

#### 4.4 Reproducibility

Three sub-samples of QVS were treated simultaneously, confirming that the experiment generated overall reproducible results. Within the weathered sample (QVS.2a, QVS.2b and QVS.2c), XRF analyses showed a RSD <5 % for bulk elements. Calcium (Ca) had a higher RSD (29 %) not accountable for by analytical errors. The deviating results may be due to slight differences in the composition of the original material, different solubility of host components caused by slight variation in temperature of the samples (Fig. 2b), or in the case of Ca the possible precipitation of gypsum in the effluent. The standard error is included in

Figs. 3 and 4 and is negligible in relation to the geochemical trends described below. For the remainder of the manuscript, the average results from the three samples are reported.

## 5. Results

### 5.1 Geochemical composition of solid material

The bulk geochemistry results highlight the differences between the BSB and QVS samples before the experiment (the pre-experiment samples will hereafter be named BSB.1 and QVS.1). BSB.1 is depleted relative to QVS.1 in elements associated with detrital material (Si, Ti, Al, Fe and K, Table 2). Total inorganic carbon content is an order of magnitude higher in BSB.1 than in QVS.1 (4.18 wt% and 0.37 wt%, respectively; Table 3). BSB.1 is enriched in TOC relative to QVS.1 (49.5 wt% and 2.61 wt%, respectively), comparable with data previously published on the Kimmeridge Blackstone band (on average 46.3 wt%, Raiswell et al., 2001). BSB.1 has a lower total Fe content and corresponding lower absolute contents of all Fe species (Table 4), with an excess of total S relative to pyrite S (Table 3). This non-pyritic S is likely bound as sulphurised organic matter (SOM) as noted by Raiswell et al. (2001). Within QVS.1, pyrite accounts for all S contained in the sample (Table 3), with no non-pyritic S. Both samples have  $\text{Fe}_{\text{HR}}/\text{Fe}_{\text{T}}$  values indicative of anoxia ( $>0.38$ ; Poulton and Canfield, 2005). BSB.1 has  $\text{Fe}_{\text{PY}}/\text{Fe}_{\text{HR}}$  values indicative of euxinia ( $>0.8$ ) whilst QVS.1 has values indicative of ferruginous depositional conditions ( $<0.7$ ).

As element contents in the samples post experiment (hereafter named BSB.2 and QVS.2) may have been affected by changes in density and overall mass loss, we compared the changes of elements of concern relative to titanium (Ti), an element which is not lost from either sample during the experiments (Table 2, S1 and S2) and which has successfully been

used in other weathering studies using similar material as a weathering-conservative element (e.g. Tuttle and Breit, 2009; Marthur et al., 2012; Jin et al., 2013; Ling et al., 2015). This generates the mass transfer coefficient ( $\tau$ , Equation 3) for monitoring loss or conservation of elements in the absence of bulk density data, as developed by Brimhall et al. (1992) (Fig. 3).

$$\tau = ((C_{j,w}/C_{j,p})/(C_{i,w}/C_{i,p})) - 1 \quad \text{Equation 3.}$$

Here the concentration of the element of concern ( $C_j$ ) is calculated as its ratio between the weathered (w) and parent (p) sample, and this is then expressed as a proportion of the ratio of the index element which is considered immobile ( $C_i$ ) in the weathered and parent sample. In this case, Ti has also been used as an index element, and it generated  $\tau$  values very similar to those calculated based on zirconium (Zr) (not reported).

Fig. 3a shows highly negative  $\tau$  values for TIC, with near 100 % loss ( $\tau$  close to -1) in QVS ( $\tau = -0.94$  in QVS, compared to -0.49 in BSB). This is matched with a loss of Ca ( $\tau = -0.36$  in QVS, compared to -0.14 in BSB), indicating loss of  $\text{CaCO}_3$  from the samples during the experiment. Total organic carbon is similarly conservative in both samples. The values of  $\tau$  are also negative for sodium (Na), magnesium (Mg) and for S, indicating notable losses of these elements. Iron values are close to 0 ( $\tau = -0.0003$  in QVS, -0.0086 in BSB), which is evidence for conservation and no significant Fe loss during the experiment. Other bulk elements (phosphorous (P), silicon (Si), aluminium (Al), manganese (Mn), potassium (K)) show values between +0.06 and -0.06, indicating only minor losses of these elements during the experiment. QVS showed a greater relative depletion of Ca, TIC, S and Mn compared to BSB.

Some differences in Fe compound content between BSB.2 and QVS.2 were found (Table 4). After the experiment, both samples showed decreases in  $\text{Fe}_{\text{Carb}}$  and  $\text{Fe}_{\text{Py}}$ , but increases in Fe

(oxyhydr)oxides (sum of  $\text{Fe}_{\text{OX}1}$  and  $\text{Fe}_{\text{OX}2}$ , Table 4, Fig. 3b). The latter is limited to the  $\text{Fe}_{\text{OX}2}$  fraction in QVS.2, whereas in BSB.2 there is an increase in both  $\text{Fe}_{\text{OX}1}$  and  $\text{Fe}_{\text{OX}2}$ . This increase is absolute, and not due to a reduction in sample mass, as evidenced by the very positive  $\tau$  values seen in Fig. 3b. These weathering-induced transformations in the Fe phase of both samples cause only minor changes in their  $\text{Fe}_{\text{HR}}/\text{Fe}_{\text{T}}$  ratios (0.07% increase for BSB, 0.03% decrease for QVS), as there is little net loss of Fe from the rock chips (Fig. 3a) and an almost quantitative switch from reduced to oxidised Fe species, as reflected by the lower  $\text{Fe}_{\text{PY}}/\text{Fe}_{\text{HR}}$  ratios in both samples (32.5% decrease in BSB, 23.1 % decrease in QVS) (Table 4).

## 5.2 Effluent composition

Over the duration of the experiment, the pH of the effluent varied between 8.9 to 9.9 for BSB and, more pronounced, from 5.3 to 8.9 for QVS (Fig. 2a). For the majority of the experiment the effluent was clear, however, in a few incidences (nine in the BSB experiment, one in the QVS experiment) a small amount of white precipitate was noted. Unfortunately, it was not possible to analyse the composition of the white precipitate, but it is known that gypsum ( $\text{CaSO}_4 \cdot 2\text{H}_2\text{O}$ ) is a common product of pyrite weathering (Forster et al., 1995) and could have reached oversaturation in the effluent. We therefore note that element concentrations analysed in the effluent samples containing precipitates are minimum estimates (in particular for Ca and S), and do not represent the full inventory of leached elements in these incidences.

To enable direct comparison of the loss of elements from the two samples into the effluents over time, we express the effluent element contents as relative percentages (rel%) of the original contents of these elements in the solid phase before the experiments (actual

concentrations available in Table S1 and S2). There are some noticeable differences in the changes of effluent composition over time, and between the BSB and QVS samples. In both samples, most Fe remained in the rock chips (loss of 0.015 rel% in BSB, 0.004 rel% in QVS Fig. 4a), while K, Al, S, Na and Mg lost between 1.0 and 7.5 rel% of their original contents into the effluent (Fig. 4b-e). Fig. 4f shows 70.6 % of original Ca was measured in the effluent from QVS and 36.5 % from BSB, providing additional evidence of Ca loss identified in the solid sample (Figure 3a). There are also some differences in the rates of loss during the duration of the experiment (Fig. 4a-h). Rates of loss tend to slow in BSB, whilst they are maintained in QVS. Cumulative S released into effluent over time as a proportion of total pyrite S available in the parent sample can be used as an approximation of the rate of pyrite oxidation. In Fig. 4g and 4h we see that the rates of loss begin to slow towards the end of the experiment in BSB (a trend not seen in QVS). These rates are likely underestimated, given the possible precipitation of S-containing minerals in the effluent.

Considering the amount (mg) of elements lost from the rock chips into solution over each time interval (Fig. 5), there does not appear to be a direct relationship between loss of S and Fe ( $r^2 < 0.01$ , Fig. 5a and b). Sulphur, however, correlates well with Ca in the effluents from both samples ( $r^2 = 0.93$  in QVS, 0.89 in BSB, Figs. 5c and d).

### 5.3 SEM-EDX analysis

When comparing rock chips from the samples before and after the experiment, there appears to be no major overall changes in either of the rock types. In BSB.2, coccolith-shaped fragments remain in faecal clusters as they were in BSB.1, and the organic matter remains concentrated in lenses (Fig. 6a and b). In QVS.2, a number of large pores are

observed that are not present in QVS.1 (Fig. 7). These could have been foraminifera plucked out in the sample preparation process, but more likely, given the evident loss of carbonate minerals during the experiment, the tests were dissolved. A white precipitate, dominated by Ca and S (measured by EDX, Fig. 5c), possibly gypsum or anhydrite, encrusts the chips in BSB.2 (Fig. 6c).

Automated heavy mineral particle analysis allows for the rapid assessment of geochemistry (via EDX) and morphology of all dense particles in SEM (brighter in BSE mode), and for a quantitative analysis of Fe:S of all Fe-containing minerals (Fig. 8). Before the experiment, both samples contained populations of particles with Fe:S ratios indicative of pyrite or other Fe sulphides (Figs. 8a, 8c, light grey and dark grey). Upon inspection of 50 randomly selected particles (in QVS.1), around 50 % of these Fe sulphides are framboidal, with the rest being present as (clusters of) euhedral crystals. Based on EDX data, the pyrite particles are subdivided into ‘pristine’ pyrite ( $\text{Fe:S} < 1$  based on apparent concentration (%)) ratio; light grey in Fig. 8) and ‘sulphur-depleted’ pyrite particles ( $\text{Fe:S} > 1$ , dark grey in Fig. 8). ‘Pristine’ pyrite particles are overall smaller in BSB.1 than in QVS.1, with an average equivalent circular diameter (ECD) of  $2 \mu\text{m}$  and an average area of  $4.4 \mu\text{m}^2$ , compared to  $2.82 \mu\text{m}$  ECD and area of  $9.36 \mu\text{m}^2$  in QVS.1. These statistical data imply a greater surface area of pyrite particles available for weathering in BSB.1. Iron (oxyhydr)oxides (Fe-rich particles with  $< 5\%$  S, black circles in Fig. 8) are often present as large (often up to  $50 \mu\text{m}$  ECD) irregular crystals in QVS.1 (Fig. 9d), and small (average ECD of  $1.3 \mu\text{m}$ ) irregularly shaped particles often associated with carbonate minerals in BSB.1 (not shown).

After the experiment, both samples show overall shifts from ‘pristine’ ( $\text{Fe:S} < 1$ ) to ‘sulphur-depleted’ ( $\text{Fe:S} > 1$ ) pyrite, and from Fe sulphides to Fe (oxyhydr)oxides or other Fe-

containing phases (with <5 wt% Fe) (Table S3, Figs. 8b, 8d). On visual inspection, these new and chemically different Fe particles, defined as ‘sulphur-depleted’ are framboids and euhedral crystals consisting of microcrystals which appear (from density comparisons) to have a pyrite core and Fe (oxyhydr)oxide rims (Fig. 9a, 9b), and thus overall lower sulphur contents. BSB shows a slightly more pronounced shift from ‘pristine’ to ‘sulphur-depleted’ particles (Table S3). Particles identified as ‘sulphur-depleted’ are concentrated around the outside of chips, in layers approximately 0.2 mm thick (Fig. 10). Some particles labelled Fe oxides in Fig. 8 are framboidal in shape (Fig. 9c). Large euhedral Fe oxides identified in QVS.1 have a mottled nature in QVS.2 (Fig. 9e).

## 6. Discussion

In both samples, Fe behaved conservatively during the experiments, and is neither leached into the effluent in any considerable quantities (Table S1, S2) nor is it lost from the samples during the experiments ( $\tau$  values very close to zero in both samples, Fig. 3a). This limited loss of Fe from a weathering shale sample is consistent with findings by Pye and Miller (1990) and Perkins and Mason (2015) as well as with natural weathering studies (Littke et al., 1991; Odin et al., 2015). Different from this study, Tuttle and Breit (2009) found Fe to be labile in naturally weathered shale, and measurements of shale weathering profiles also show negative  $\tau$  values for Fe (Marcellus Shale  $\tau$  up to -0.27 (Jin et al., 2013); Rose Hill Shale maximum  $\tau$  -0.51 to -0.77 (Jin et al., 2013; Brantley et al., 2013). Iron was also released from shales into experimental leachate solutions, as reported by Lierman et al. (2011), Bhatti (2015), and Perkins and Mason (2015).

Natural variability in the permeability of the shales, as well as climate and period of time exposed to the ambient climate could account for some of these differences. However, the geochemical composition of the shales has been implicated in different weathering scenarios for Fe in previous studies. Tuttle and Breit (2009) and Brantley et al. (2013) suggested that low pH conditions and the lack of carbonate buffering were responsible for the dissolution and removal of most Fe-containing pyrite weathering products. In contrast, it has been shown that neutral to alkaline pH inhibits pyrite oxidation in laboratory experiments (Nordstrom, 1982; Nicholson et al., 1988), in soils (Lara et al., 2015), in acid mine drainage situations (Wiggering, 1993; Evangelou and Zhang, 1995; Huminicki and Rimstidt, 2009), and when storing wet shale samples (Kraal et al., 2009). In this study, the most notable change in the geochemical composition of shale samples after the experiment is the dissolution of carbonates. Fig. 3a shows that TIC and Ca are significantly depleted from both shale samples following the experiment, suggesting almost complete loss of  $\text{CaCO}_3$  from QVS.2, supported also by the high amounts of Ca present in the effluent (Fig. 4f). The relative instability of carbonate (calcite) during shale weathering has been noted in previous experiments (e.g. Ritsema and Groenenberg, 1993; White et al., 2005) and field observations (e.g. Brantley et al., 2013). This, and the resultant release of  $\text{HCO}_3^-$  (Equation 2), are contributing factors to the increasing and ultimately slightly alkaline pH values in the effluents of both experiments (Fig. 2a), which is different to previous shale weathering experiments where the pH was often much lower (e.g. Liao et al., 2014, pH 4.2-6.0; Bhatti, 2015, pH 1.2-2.2; Perkins and Mason, 2015, pH 3.6-6.2). The reason for this divergence in pH is that earlier experiments either removed carbonate from the shale samples prior to the artificial weathering or used shales that were initially very low in Ca (and so presumably low in carbonate). A correlation between Ca and S in the effluents of both samples (Fig. 5c and

5d) and the identification of calcium sulphur compounds on the edges of BSB.2 rock chips hint at the formation of gypsum, a common product of carbonate dissolution driven by pyrite oxidation (Forster et al., 1995).

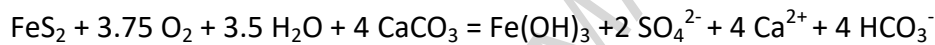
At neutral to alkaline pH, as in this experiment, one of the intermediate products of pyrite oxidation, ferric hydroxide, precipitates in the shale pore spaces (Nordstrom, 1982). As Fe<sup>3+</sup> is also an oxidant, removing it from solution by precipitation of ferric hydroxide (which is particularly important in the low O<sub>2</sub> environments likely in mudrock pores) would also likely slow pyrite oxidation (Rimstidt and Newcomb, 1993; Chandra and Gerson, 2010). In experiments where pyrite was weathered in the presence of carbonate, and thus in higher pH environments (Nicholson et al., 1988; Lara et al., 2015), the build-up of Fe (oxyhydr)oxides on pyrite surfaces caused decreasing rates of pyrite oxidation, due to the shrinking core model. In this model, rates of pyrite oxidation are limited by the rate of oxygen diffusion through the build-up of the oxidation products around the edge of a particle (Nicholson et al., 1990). The microscopic evidence for Fe (oxyhydr)oxide rims around pyrite cores on individual ‘sulphur-depleted’ microcrystals in post experiment samples (Figs. 9a, 9b) supports this model of rate limitation in carbonate-containing shale (Fig. 11). Since the Fe (oxyhydr)oxides are relatively stable compared to pyrite under prevailing weathering conditions (Schwertmann and Taylor, 1989), ‘sulphur-depleted’ pyrite particles are essentially ‘passivated’ by Fe (oxyhydr)oxide coatings. ‘Armouring’ of minerals was proposed to explain why experiments using powder and weathering models required unusually small surface areas to force modelling results to match field observations of pyrite oxidation (Heidari et al., 2017) and these ‘passivated’ pyrite grains may be an example of this armouring.

Quantitative data produced by the SEM EDX technique also allow for a comparison of ‘passivation’ in QVS and BSB (Table S3). Compared to QVS, there was a more pronounced shift from ‘pristine’ to ‘sulphur-depleted’ pyrite (Table S3) during the experiment within BSB, combined with a more pronounced increase in the  $\text{Fe}_{\text{Ox1}}$  pool identified by sequential Fe extraction (Table 4). This, coupled with a slowing rate of S and Ca removal into the effluent (Figs. 4a, b, c) in BSB compared to QVS (where Ca and S removal continues at similar rates until the end of the experiment) could suggest decreasing pyrite oxidation and carbonate dissolution, hinting at enhanced pyrite ‘passivation’.

This more significant ‘passivation’ in BSB could have a number of reasons linked to factors controlling rates of pyrite oxidation seen in other studies. (A) Higher surface area for pyrite oxidation and Fe (oxyhydr)oxide precipitation to take place (Chandra and Gerson, 2010; Heidari et al., 2017); in both BSB.1 and BSB.2, pyrite grains had a smaller average ECD than in QVS.1 and QVS.2; (B) The flow rate of oxygenated water (Heidari et al., 2017), linked to permeability, may also have been higher in BSB samples, however, there are no data available to compare flow rates in the two samples; (C) the slightly higher temperature in the BSB experiment which was carried out in the summer (Fig. 2a); or (D) the higher pH in BSB.1, especially within pH buffered microenvironments caused by carbonate dissolution amongst the coccolithophore debris (Fig. 6), allowed more pervasive precipitation of  $\text{Fe}^{3+}$  than in QVS, where pH of the effluent and carbonate concentrations within the sample were much lower, and eventually most carbonate had been dissolved.

As  $\text{CaCO}_3$  is efficient at consuming  $\text{H}^+$  ions from pyrite oxidation, thereby buffering acidic solutions, Brantley et al. (2013) suggested calculating an R value (stoichiometrically derived from Equation 4) to calculate if all acid generated by pyrite oxidation can be consumed by

$\text{CaCO}_3$  dissolution. Values for both parent samples are below 1, suggesting that there is sufficient  $\text{CaCO}_3$  to consume any acid produced by pyrite oxidation, minimising the effect of this acid on any other minerals. Therefore, losses of Na from our shale samples might be due to desorption from clay minerals and not from acid hydrolysis of aluminosilicates (Pye and Miller, 1990). R values are an order of magnitude lower for BSB.1, because of the higher  $\text{CaCO}_3$  content (QVS.1 0.15, BSB.1 0.01). We suggest that if pyrite passivation is occurring in samples where carbonates are dissolving, R values of <1 may mean weathering is limited not only by the amount of acid available for weathering reactions, but also by pyrite ‘passivation’. There may be an optimum R value for pyrite ‘passivation’ in shales (close to the R value in BS), which could be further investigated taking advantage of the quantitative observations in SEM EDX.



$$R = M_{\text{PYR}} / 4M_{\text{CaCO}_3}$$
Equation 4 (From Brantley et al., 2013)

In both samples studied, the pyrite framboids indicate the same process of *in situ* Fe phase transformation from sulphides to (oxyhydr)oxides via diffusion at individual pyrite microcrystal surfaces, with little change in framboid morphology. The retention of pyrite framboid (and euhedral) morphology during pyrite ‘passivation’ seen in Figs. 9a and 9b may be due to the two-stage oxidation process suggested by Huminicki and Rimstidt (2009). In that model, dissolved Fe forms poorly crystalline Fe (oxyhydr)oxide colloids which are attracted to the pyrite surface, forming a semi-permeable layer which encourages the precipitation of further Fe (oxyhydr)oxide between the pyrite surface and this colloidal layer. There is even evidence that some pyrite particles have been almost completely oxidised retaining the original framboid morphology (Fig. 9c). The preservation of pyrite

(particularly framboid) morphology has also been identified in various palaeo-redox studies which use outcrop samples (Luning et al., 2003; Wignall et al., 2005; Stebbins et al., 2019).

In terms of weathering overprints on palaeo-redox indicators, the observed changes in Fe phase (dissolution of  $\text{Fe}_{\text{CARB}}$ , oxidation of  $\text{Fe}_{\text{PY}}$  and formation of  $\text{Fe}_{\text{OX}}$ ) do not significantly affect the  $\text{Fe}_{\text{HR}}/\text{Fe}_{\text{T}}$  proxy as the Fe (oxyhydr)oxide products of pyrite oxidation ( $\text{Fe}_{\text{OX1}}$  and  $\text{Fe}_{\text{OX2}}$ ) are also part of the  $\text{Fe}_{\text{HR}}$  pool. Also, it appears that Fe-rich clay minerals (Fe species not considered as  $\text{Fe}_{\text{HR}}$ , defined here as  $\text{Fe}_{\text{PRS}}$ ) reported to form or being lost in natural weathering profiles (Caillaud et al., 2004; Heidari et al., 2017) are not being impacted on the timescale or the setup used in our experiment. Therefore, we conclude that the  $\text{Fe}_{\text{HR}}/\text{Fe}_{\text{T}}$  proxy can be reliably used in outcrop samples which have been exposed to oxygen and water for a limited amount of time, and where the transformation from pristine to ‘sulphur depleted’ pyrite has taken place. Different from the  $\text{Fe}_{\text{HR}}/\text{Fe}_{\text{T}}$  ratio, the  $\text{Fe}_{\text{PY}}/\text{Fe}_{\text{HR}}$  ratio was significantly modified during the experiment (Table 4). Loss of pyrite is evident from negative  $\tau_{\text{Fe}_{\text{PY}}}$  and S values (Fig. 3c), and S has leached into the effluents of both samples (Fig. 4g). Much more sulphur leached into the effluent than Fe (Figs. 3b, 4g, 5a, 5b; Table S1, S2), although there is some evidence of S-containing weathering products being retained in the rock, precipitating on the edge of rock chips as gypsum (Fig. 6c.). This reduction in  $\text{Fe}_{\text{PY}}/\text{Fe}_{\text{HR}}$  in the shale samples would affect the interpretation of the hydrogen sulphide availability in the palaeo-depositional environment in the BSB sample, changing it from euxinic ( $>0.8$ ) pre-experiment to ferruginous ( $<0.7$ ) post experiment (Poulton and Canfield, 2011), therefore this proxy may be less reliable in weathered shale samples.

In BSB, the non-pyrite S fraction (Fig. 3c), assumed to be predominately sulphurised organic matter (Raiswell et al., 2001), remained unchanged ( $\tau$  values close to zero) during the

experiment. This is likely due to the conservative nature and oxidation resistance of sulphurised organic matter (Table 3), supporting previous findings by Petsch (2000). However, the possible formation of gypsum, some of which was retained within the rock chips analysed (Fig. 6c), will have also added to the non-pyritic sulphur pool. In both samples, TOC contents appeared to be stable over the course of the experiment (positive  $\tau$  values, Fig. 3a), supporting previous research that organic carbon compounds are relatively stable against weathering when compared to pyrite (Clayton and Swetland, 1978; Petsch, 2000). In addition, as both P and TOC are conservative in this experiment (Fig. 3a), the TOC/P redox palaeoproxy (Ingall et al., 1993) also appears to be resistant to oxidative weathering. Although the P containing mineral apatite is susceptible to acidic dissolution, it likely becomes associated with newly formed Fe (oxyhydr)oxides (Kraal et al., 2009) and so values within the bulk sediment are unaffected.

## **7. Implications and Conclusions**

This weathering experiment was not designed to replicate natural weathering conditions, but rather to stimulate some of the most common geochemical transformations taking place during shale weathering, and to observe the effects on common palaeo-redox proxies. The experiment caused leaching of carbonate minerals, oxidation of pyrite (decrease in pyrite identified in wet chemical extractions and the identification of 'sulphur depleted' pyrite particles), and possible production of gypsum (identified in SEM EDX) and Fe (oxyhydr)oxides as secondary precipitates. We therefore show that the relatively simple soxhlet setup selected in this study has caused reactions observed in more complicated weathering experiments and in natural systems. With the benefit of SEM EDX elemental

mapping, it is possible to observe the spatial extent of these weathering reactions (Fig. 10). Despite the short duration of the experiment (four weeks), the affected pyrite particles can be observed on average 0.2 mm into each shale chip, suggesting a weathering/penetration rate of O<sub>2</sub> and water of around 0.2 mm/month. Although more detailed work would be required to make a direct comparison between the laboratory experiment and field weathering rates, the laboratory experiment rates are likely to be faster, due to the higher temperatures involved, larger surface area and the complete exchange of weathering fluids. The 0.2mm/month is therefore relevant as it is orders of magnitude lower than reported physical erosion rates calculated for high physical denudation situations, including mountainous stream beds (mm to cm/yr Hsieh and Knuepfer, 2001; Cornwell et al., 2003) and coastal cliffs (m/yr, Rosser et al., 2005), which are often selected for sampling for geochemical studies. As the Fe<sub>HR</sub>/Fe<sub>T</sub> proxy appears to be relatively conservative during weathering on such timescales, high erosion rates would mean that affected QVS rocks in the Quebrada Vara Santa stream outcrop and the BSB cliff in Clavell's Hard would be physically eroded before these proxies would become unreliable.

Iron appears to be more conservative when our  $\tau$  values are compared to those in natural weathering studies. If, as suggested by some authors (e.g. Tuttle and Breit, 2009; Brantley et al., 2013), higher pH values reduce the rates of pyrite oxidation by precipitating Fe (oxyhydr)oxides as rims on pyrite particles, this may suggest that rocks containing a certain amount of CaCO<sub>3</sub> (with an R value significantly less than 1) may be considered more reliable for Fe<sub>HR</sub>/Fe<sub>T</sub> (and P/TOC) proxies for reconstructing redox in the water column. Supporting this, Kraal et al. (2009) noted that drill core samples were less prone to pyrite oxidation if they contained more than 5% CaCO<sub>3</sub>. This mechanism for limiting pyrite oxidation may also affect other geochemical proxies. Since some redox-sensitive/sulphide-forming trace

elements (e.g. Ni, Cu, Mo and Zn) are known to be associated with pyrite (Huerta-Diaz and Morse, 1992; Gregory et al. 2015), their mobility during outcrop weathering should be determined by the degree of pyrite oxidation (Zhu et al., 2008; Perkins and Mason, 2015), and loss could be limited by pyrite ‘passivation’.

Geochemical identification and quantification of ‘sulphur depleted’ oxidised pyrite particles presented here provide a novel addition to the geochemical toolbox for quantifying pyrite oxidation and the extents of weathering. This could fill a gap in natural weathering studies, where quantification of weathering is often difficult as the geochemistry of the parent rock required for  $\tau$  calculations (Equation 3) is difficult to assign (Jin et al., 2013; Brantley et al., 2013). Also, when applying the  $\text{Fe}_{\text{PY}}/\text{Fe}_{\text{HR}}$  proxy to infer ferruginous/euxinic conditions from outcrop samples we recommend SEM EDX analyses to confirm the absence of affected pyrite particles, building confidence that geochemical interpretations were robust. The results reported in this paper invite further study into the nature (including high resolution geochemical analysis like time of flight secondary ion mass spectrometry (ToF-SIMS) and long-term fate of ‘passivated’ pyrite particles, in order to investigate this effect on the use of geochemical proxies at outcrop, trace element contamination of drinking waters, and geological scale effect on the sulphur cycle.

## Acknowledgements

This work was undertaken with a generous grant from Ecopetrol S.A. and Newcastle University. Geochemical analysis was carried out at Newcastle University. XRF was carried out at the ICBM, Oldenburg University by Dr. Bernhard Schnetger and his team. We would also like to thank two anonymous reviewers, whose comments contributed significantly to the finished manuscript.

## References

- Armstrong, H.A., Wagner, T., Herringshaw, L.G., Farnsworth, A.J., Lunt, D.J., Harland, M., Imber., J, Lopton, C., Atar, E.F., 2016. Hadley circulation and precipitation changes controlling black organic-rich mudrock deposition in the Late Jurassic Boreal Seaway. *Palaeoceanography* 31(8), 1041-1053.
- Berner, R.A., Raiswell, R., 1984. C/S method for distinguishing freshwater from marine sedimentary rocks. *Geology* 12(6), 365-368. Bhatti, T. M., 2015. Bioleaching of organic carbon rich polymetallic black organic-rich mudrock. *Hydrometallurgy* 157, 246-255.
- Blanco, V. 2012. Modelling and geochemical characterization of organic facies in the Upper Cretaceous Chipaque Formation, Eastern Cordillera and Llanos Foothills, Colombia. (MSc thesis). Newcastle University, UK.
- Bolin, T.B., Birdwell, J.E., Lewan, M.D., Hill, R.J., Grayson, M.B., Mitra-Kirtley, S., Bake, K.D., Craddock, P.R., Abdallah, W., Pomerantz, A.E., 2016. Sulfur Species in Source Rock Bitumen before and after Hydrous Pyrolysis Determined by X-ray Absorption Near-Edge Structure. *Energy & Fuels* 30(8), 6264-6270.

Brantley S.L., White A.F., 2009. Chapter 10. Approaches to modeling weathered regolith.

Thermodynamics and kinetics of water-rock interaction. *Reviews in Mineralogy and*

*Geochemistry* 70 (1), 435-484.

Brantley, S.L., Holleran, M.E., Jin, L., Bazilevskaya, E., 2013. Probing deep weathering in the Shale Hills Critical Zone Observatory, Pennsylvania (USA): the hypothesis of nested chemical reaction fronts in the subsurface. *Earth Surface Processes and Landforms* 38(11), 1280-1298.

Brantley, S.L., Lebedeva, M.I., Balashov, V.N., Singha, K., Sullivan, P.L., Stinchcomb, G., 2017. Toward a conceptual model relating chemical reaction fronts to water flow paths in hills. *Geomorphology* 277, 100-117.

Brimhall, G.H., Chadwick, O.A., Lewis, C.J., Compston, W., Williams, I.S., Danti, K.J., Dietrich, W.E., Power, M.E., Hendricks, D., Bratt, J., 1992. Deformational mass transport and invasive processes in soil evolution. *Science* 255(5045), 695-702.

Brumsack, H.J., 2006. The trace metal content of recent organic carbon-rich sediments: implications for Cretaceous black shale formation. *Palaeogeography, Palaeoclimatology, Palaeoecology* 232(2-4), 344-361.

Buckman, J., Mahoney, C., Bankole, S., Couples, G., Lewis, H., Wagner, T., Stow, D., 2018. Workflow model for the digitization of mudrocks. *Geological Society, London, Special Publications* 484, SP484-2.

Caillaud, J., Proust, D., Righi, D., Martin, F., 2004. Fe-rich clays in a weathering profile developed from serpentinite. *Clays and Clay Minerals* 52(6), 779-791.

- Camp, W., Diaz, E., Wawak, B., 2013. Introduction to Memoir. In: Camp, W., Diaz, E., Wawak, B., (Eds), Electron microscopy of shale hydrocarbon reservoirs: AAPG Memoir 102. American Association of Petroleum Geologists, Bath, UK, pp. 53-66
- Canfield, D.E., Raiswell, R., Westrich, J.T., Reaves, C.M., Berner, R.A., 1986. The use of chromium reduction in the analysis of reduced inorganic sulfur in sediments and shales. *Chemical Geology* 54(1-2), 149-155.
- Chandra, A.P., Gerson, A.R., 2010. The mechanisms of pyrite oxidation and leaching: a fundamental perspective. *Surface Science Reports* 65(9), 293-315.
- Clayton, J.L., Swetland, P.J., 1978. Subaerial weathering of sedimentary organic matter. *Geochimica et Cosmochimica Acta* 42(3), 305-312.
- Cornwell, K., Norsby, D., Marston, R., 2003. Drainage, sediment transport, and denudation rates on the Nanga Parbat Himalaya, Pakistan. *Geomorphology* 55(1), 25-43.
- Eckert, S., Brumsack, H.J., Severmann, S., Schnetger, B., März, C., Fröllje, H., 2013. Establishment of euxinic conditions in the Holocene Black Sea. *Geology* 41(4), .431-434.
- Evangelou, V.P., Zhang, Y.L., 1995. A review: pyrite oxidation mechanisms and acid mine drainage prevention. *Critical Reviews in Environmental Science and Technology* 25(2), 141-199.
- Forster, A., Culshaw, M.G., Bell, F.G., 1995. Regional distribution of sulphate in rocks and soils of Britain. *Geological Society, London, Engineering Geology Special Publications* 10(1), 95-104.

Gregory, D.D., Large, R.R., Halpin, J.A., Baturina, E.L., Lyons, T.W., Wu, S., Bull, S.W., 2015.

Trace element content of sedimentary pyrite in black shales. *Economic Geology* 110(6), 1389-1410.

Heidari, P., Li, L., Williams, J.Z., Brantley, S.L., 2017. A reactive transport model for Marcellus shale weathering. *Geochimica et Cosmochimica Acta* 217, 421-440.

Huerta-Diaz, M.A., Morse, J.W., 1992. Pyritization of trace metals in anoxic marine sediments. *Geochimica et Cosmochimica Acta* 56(7), 2681-2702.

Huminicki, D.M., Rimstidt, J.D., 2009. Iron oxyhydroxide coating of pyrite for acid mine drainage control. *Applied Geochemistry* 24(9), 1626-1634.

Hsieh, M.L., Knueper, P.L., 2001. Middle–late Holocene river terraces in the Erhjen River Basin, southwestern Taiwan—Implications of river response to climate change and active tectonic uplift. *Geomorphology* 38(3), 337-372.

Jeng, A.S., 1992. Weathering of some Norwegian alum shales, II. Laboratory simulations to study the influence of aging, acidification and liming on heavy metal release. *Acta Agriculturae Scandinavica B-Plant Soil Sciences* 42(2), 76-87.

Jin, L., Mathur, R., Rother, G., Cole, D., Bazilevskaya, E., Williams, J., Brantley, S. 2013. Evolution of porosity and geochemistry in Marcellus Formation black shale during weathering. *Chemical Geology* 356, 50-63.

Kraal, P., Slomp, C.P., Forster, A., Kuypers, M.M., Sluijs, A., 2009. Pyrite oxidation during sample storage determines phosphorus fractionation in carbonate-poor anoxic sediments. *Geochimica et Cosmochimica Acta* 73(11), 3277-3290.

Lara, R.H., Monroy, M.G., Mallet, M., Dossot, M., González, M.A., & Cruz, R., 2015. An experimental study of iron sulfides weathering under simulated calcareous soil conditions. *Environmental Earth Sciences* 73(4), 1849-1869.

Liao, X., Chigira, M., Matsushi, Y., Wu, X., 2014. Investigation of water–rock interactions in Cambrian black organic-rich mudrock via a flow-through experiment. *Applied Geochemistry* 51, 65-78.

Liermann, L.J., Mathur, R., Wasylewski, L.E., Nuester, J., Anbar, A.D., Brantley, S.L., 2011. Extent and isotopic composition of Fe and Mo release from two Pennsylvania shales in the presence of organic ligands and bacteria. *Chemical Geology* 281(3-4), 167-180.

Ling, S., Wu, X., Ren, Y., Sun, C., Liao, X., Li, X., Zhu, B., 2015. Geochemistry of trace and rare earth elements during weathering of black shale profiles in Northeast Chongqing, Southwestern China: their mobilization, redistribution, and fractionation. *Chemie der Erde-Geochemistry* 75(3), 403-417.

Littke, R., Klussmann, U., Krooss, B., Leythaeuser, D., 1991. Quantification of loss of calcite, pyrite, and organic matter due to weathering of Toarcian black shales and effects on kerogen and bitumen characteristics. *Geochimica et Cosmochimica Acta* 55(11), 3369-3378.

Luning, S., Kolonic, S., Loydell, D.K., Craig, J., 2003. Reconstruction of the original organic richness in weathered Silurian shale outcrops (Murzuq and Kufra basins, southern Libya). *Geoarabia-Manama* 8, 299-308.

Mathur, R., Jin, L., Prush, V., Paul, J., Ebersole, C., Fornadel, A., Williams, J.Z., Brantley, S., 2012. Cu isotopes and concentrations during weathering of black shale of the Marcellus Formation, Huntingdon County, Pennsylvania (USA). *Chemical Geology* 304, 175-184.

Negri, A., Wagner, T., Meyers, P.A., 2006. Introduction to "Causes and consequences of organic carbon burial through time". *Palaeogeography, Palaeoclimatology, Palaeoecology*, 235, 1-7.

Nicholson, R.V., Gillham, R.W., Reardon, E.J. 1988. Pyrite oxidation in carbonate-buffered solution: 1. Experimental kinetics. *Geochimica et Cosmochimica Acta* 52(5), 1077-1085.

Nicholson, R.V., Gillham, R.W., Reardon, E.J., 1990. Pyrite oxidation in carbonate-buffered solution: 2. Rate control by oxide coatings. *Geochimica et Cosmochimica Acta* 54(2), 395-402.

Nordstrom, D.K., 1982. Aqueous pyrite oxidation and the consequent formation of secondary iron minerals. In: J.A. Kittrick, D.S. Fanning, L.R. Hossner (Eds.), Acid sulfate weathering. Soil Society of America Special Publication vol 10, Madison, WI, pp. 37-56

Odin, G.P., Cabaret, T., Mertz, J.D., Menendez, B., Etienne, L., Wattiaux, A., Rouchon, V., 2015a. Alteration of fossil-bearing shale (Autun Basin, France; Permian), part I: Characterizing iron speciation and its vulnerability to weathering by combined use of Mössbauer spectroscopy, X-ray diffraction, porosimetry and permeability measurements. *Annales de Paléontologie*, 101( 2), 75-85.

Odin, G.P., Vanmeert, F., Farges, F., Gand, G., Janssens, K., Romero-Sarmiento, M.F., Steyer, J. S., Vantelon, D., Rouchon, V., 2015b. Alteration of fossil-bearing shale (Autun, France; Permian), part II: Monitoring artificial and natural ageing by combined use of S and Ca K-edge XANES analysis, Rock-Eval pyrolysis and FTIR analysis. *Annales de Paléontologie* 101(3), 225-239.

- Pedro, G., 1961. An experimental study on the geochemical weathering of crystalline rocks by water. *Clay Minerals Bulletin* 4(26), 266-281.
- Perkins, R.B., Mason, C.E., 2015. The relative mobility of trace elements from short-term weathering of a black shale. *Applied Geochemistry* 56, 67-79.
- Petsch, S.T., Berner, R.A., Eglinton, T.I., 2000. A field study of the chemical weathering of ancient sedimentary organic matter. *Organic Geochemistry* 31(5), 475-487.
- Poulton, S.W., Krom, M.D., Raiswell, R., 2004. A revised scheme for the reactivity of iron (oxyhydr) oxide minerals towards dissolved sulfide. *Geochimica et Cosmochimica Acta* 68(18), 3703-3715.
- Poulton, S.W., Canfield, D.E., 2005. Development of a sequential extraction procedure for iron: implications for iron partitioning in continentally derived particulates. *Chemical Geology* 214(3), 209-221.
- Poulton, S.W., Canfield, D.E., 2011. Ferruginous conditions: a dominant feature of the ocean through Earth's history. *Elements* 7(2), 107-112.
- Poulton, S.W., Henkel, S., März, C., Urquhart, H., Flögel, S., Kasten, S., Wagner, T. 2015., A continental-weathering control on orbitally driven redox-nutrient cycling during Cretaceous Oceanic Anoxic Event 2. *Geology* 43(11), 963-966.
- Pye, K., Miller, J.A., 1990. Chemical and biochemical weathering of pyritic mudrocks in a shale embankment. *Quarterly Journal of Engineering Geology and Hydrogeology* 23(4), 365-382.

Raiswell, R., Buckley, F., Berner, R.A., Anderson, T.F., 1988. Degree of pyritization of iron as a paleoenvironmental indicator of bottom-water oxygenation. *Journal of Sedimentary Research* 58(5), 812-819.

Raiswell, R., Newton, R., Wignall, P.B., 2001. An indicator of water-column anoxia: resolution of biofacies variations in the Kimmeridge Clay (Upper Jurassic, UK). *Journal of Sedimentary Research* 71(2), 286-294.

Raiswell, R., Canfield, D.E., 2012. The iron biogeochemical cycle past and present. *Geochemical perspectives*, 1(1), pp.1-2.

Rimstidt, J.D., Newcomb, W.D., 1993. Measurement and analysis of rate data: The rate of reaction of ferric iron with pyrite. *Geochimica et Cosmochimica Acta* 57(9), 1919-1934.

Ritsema, C.J., Groenenberg, J.E., 1993. Pyrite oxidation, carbonate weathering, and gypsum formation in a drained potential acid sulfate soil. *Soil Science Society of America Journal* 57(4), 968-976.

Rosser, N.J., Petley, D.N., Lim, M., Dunning, S.A., Allison, R.J., 2005. Terrestrial laser scanning for monitoring the process of hard rock coastal cliff erosion. *Quarterly Journal of Engineering Geology and Hydrogeology* 38(4), 363-375.

Schillawski, S., Petsch, S., 2008. Release of biodegradable dissolved organic matter from ancient sedimentary rocks. *Global Biogeochemical Cycles*, 22(3).

Schwertmann, U., Taylor, R.M., 1989. Iron oxides. In: J.B.Dixon, S.B.Weed (Eds.), *Minerals in soil environments*. Soil Science Society of America, Madison, WI, USA, pp. 379-438.

Senkayi, A.L., Dixon, J.B., Hossner, L.R., 1981. Simulated weathering of lignite overburden shales from Northeast Texas. *Soil Science Society of America Journal* 45(5), 982-986.

Stebbins, A., Williams, J., Brookfield, M., Nye Jr, S.W., Hannigan, R., 2019. Frequent euxinia in southern Neo-Tethys Ocean prior to the end-Permian biocrisis: Evidence from the Spiti region, India. *Palaeogeography, Palaeoclimatology, Palaeoecology* 516, 1-10.

Tribouillard, N., Riboulleau, A., Lyons, T., Baudin, F. 2004., Enhanced trapping of molybdenum by sulfurized marine organic matter of marine origin in Mesozoic limestones and shales. *Chemical Geology* 213(4), 385-401.

Tuttle, M.L., Breit, G.N., 2009. Weathering of the New Albany Shale, Kentucky, USA: I. Weathering zones defined by mineralogy and major-element composition. *Applied Geochemistry* 24(8), 1549-1564.

Washburn, K.E., Birdwell, J.E., 2013. Multivariate analysis of ATR-FTIR spectra for assessment of oil organic-rich mudrock organic geochemical properties. *Organic geochemistry* 63, 1-7.

Wedepohl, K.H., 1971. Environmental influences on the chemical composition of shales and clays. *Physics and Chemistry of the Earth* 8, 307-333.

Wedepohl, K.H., 1991. The composition of the upper earth's crust and the natural cycles of selected metals. *Metals in natural raw materials. Natural Resources*. In: Merian, E.(Ed.), *Metals and Their Compounds in the Environment*. John Wiley and Sons, New York, USA, pp. 3-17.

White, A.F., Schulz, M.S., Lowenstern, J.B., Vivit, D.V., Bullen, T.D., 2005. The ubiquitous nature of accessory calcite in granitoid rocks: implications for weathering, solute evolution, and petrogenesis. *Geochimica et Cosmochimica Acta* 69(6), 1455-1471.

- Wiggering, H., 1993. Sulfide oxidation—an environmental problem within colliery spoil dumps. *Environmental Geology* 22(2), 99-105.
- Wignall, P.B., Newton, R., Brookfield, M.E., 2005. Pyrite framboid evidence for oxygen-poor deposition during the Permian–Triassic crisis in Kashmir. *Palaeogeography, Palaeoclimatology, Palaeoecology* 216(3), 183-188.
- Wildman, R.A., Berner, R.A., Petsch, S.T., Bolton, E.W., Eckert, J.O., Mok, U., Evans, J.B., 2004. The weathering of sedimentary organic matter as a control on atmospheric O<sub>2</sub>: I. Analysis of a black shale. *American Journal of Science* 304(3), 234-249.
- Zhu, W., Young, L.Y., Yee, N., Serfes, M., Rhine, E.D., Reinfelder, J. R., 2008. Sulfide-driven arsenic mobilization from arsenopyrite and black shale pyrite. *Geochimica et Cosmochimica Acta* 72(21), 5243-5250.
- Zhu, B., Wu, X., 2012. Weathering process of black strata and formation of corrosive environmental water. *Procedia Environmental Sciences* 12, 984-990.

### **Figure Captions**

Figure 1. Experimental set-up, with modified soxhlet extractor. Modified from Pedro et al., 1961.

Figure 2. Measurements taken during the experiment. a. pH measured within effluent during sampling. b. Temperature measured within the sample thimble. Error bars are standard error measured in three replicate experiments. Open circles are QVS, closed circles are BSB.

Figure 3. Mass transfer coefficient of elements and Fe species calculated using Equation 3, with Ti as the index element, used to compare element contents in the original and treated sample (after 4 weeks). Positive values indicate conservation, negative values indicate loss. Complete loss is indicated by a mass transfer coefficient of -1. Black bars are BSB, white bars are QVS. Error bars are standard error of three replicated experiments. Figure a. shows mass transfer coefficients of the bulk elements determined by XRF (apart from TOC, TIC and S from LECO and CNS analysis). Figure b. shows mass transfer coefficients of Fe compounds determined by sequential extraction and chromous chloride reduction.

Figure 4. Percentage of element available in the solid samples before the experiment which has leached into effluent (cumulative mg leached into effluent as a percentage of mg of element in original sample, cumulative rel(%)). Figure h. is cumulative mg S leached into effluent as a percentage of mg in pyrite measured by chromous reduction. Open circles are QVS (error bars are the standard error of three replicates). Closed circles are BSB. Diamonds seen in Figures f., g. and h. are incidences where a precipitate was present in the effluent.

Figure 5. Correlations between concentrations of elements within the effluent samples (mg/l). Open data points (a and c) are from QVS (one sample chosen from the three experiments but all show similar trends) and closed data points (b. and d.) are from BSB.

Figure 6. SEM BSE imagery of randomly selected chips from BSB.1 (a.) and BSB.2 (b.). Features visible in these images include faecal pellets comprised of coccolith fragments, black material which is likely organic matter and pyrite. A coating of a mineral with high concentrations of Ca and S (possibly gypsum) is noted on the outside of a chip from BSB.2 (c.).

Figure 7. SEM BSE imagery of randomly selected chips from QVS.1 (a) to QVS.2 (b). Quartz, pyrite, Fe oxyhydr(oxides) and carbonate minerals are identified.

Figure 8. SEM EDX elemental data with each data point showing the Fe and S concentration (in apparent %) of individual bright particles analysed by automated particle analysis of a thin section of BSB chips. Figure a. is pre-experiment BSB.1 and b. is post-experiment BSB.2, c. is pre experiment QVS.1 and d. is post experiment QVS.2. Black crosses are <5% Fe, light grey are particles with a Fe content >5% and Fe:S ratio less than 1 and are considered ‘pristine’ pyrite. Dark grey data points have a Fe:S ratio greater than 1 and have more than 5% S. Black circles contain less than 5% S and are considered to be Fe oxides. Modified from Buckman et al., 2018

Figure 9. SEM Back scattered electron (BSE) images, examples of Fe particles and weathering products. Images a., b., c. and e. from QVS.2, post experiment. Image d. is from QVS.1. Images b. and c. are taken from Buckman et al., 2018. Pyrite is characteristically bright in BSE whereas Fe oxide rims are darker. Note rims around pyrite in b. have a similar brightness to Fe oxide framboid in c., providing evidence for their similar density and composition.

Figure 10. Aztec generated image of automated particle data of BSB.2 combining EDX chemical data with SEM imagery. Clearly visible are ‘sulphur-depleted’ pyrite particles (those with  $\text{Fe:S} > 1$ ) in yellow concentrated around the outside of the chips and ‘pristine’ pyrite particles (with  $\text{Fe:S} < 1$ ) in red concentrated in the centre of each chip. Modified from Buckman et al., 2018

Figure 11. Conceptual model of shrinking core model as seen in SEM BSE imagery of pyrite framboids in QVS.2 (adapted from Nicholson et al., 1990). This model implies the products of

pyrite oxidation (Fe(oxhydr)oxides) build up on the pyrite particle, minimising the penetration of O<sub>2</sub> and water for further pyrite oxidation. Image modified from Buckman et al., 2018.

### Table Captions

Table 1. Extraction scheme for Fe-speciation taken from Poulton and Canfield, 2005. All extractions at 25°C unless stated otherwise. Details of chromous chloride distillation described in Canfield et al., 1986.

Table 2. Bulk geochemistry analysed via XRF in pre-experiment samples and post-experiment samples (shaded grey). Averages of three samples are shown for QVS.2, with standard error in brackets.

Table 3. Bulk geochemistry (Total organic carbon (TOC), Total inorganic carbon (TIC)), analysed via LECO and CNS analyser, with PyS (pyrite S) analysed via chromium reduction methods. Non-PyS is calculated from total S minus PyS Pre-experiment samples and post-experiment samples (shaded grey). Averages of three samples are shown for QVS.2, with standard error in brackets.

Table 4. Results of Fe compound determination on the two studied samples before and after (shaded) experiment in wt%. QVS.2 is average (n=3) with standard error in brackets.

### Supplementary Material

Table S1. Concentrations of elements in the effluent during experiment on BSB as measured by ICP-OES. Values in italic are below the limits of quantification.

Table S2. Concentrations of elements in the effluent during experiment of an example QVS sample as measured by ICP-OES. Values in italic are below the Limits of quantification (LOQ).

Table S3. Presenting information shown in Figure 8 and 9 in a numerical format with proportions and actual numbers of particles in brackets. On the left, relative proportions are calculated only from particles with chemical compositions indicating Fe sulphides (particles with >5 % S), highlighting the shift to sulphur-depleted pyrite after the experiment. On the right, all Fe-containing particles are included, to show the increase in Fe (oxyhydr)oxides (particles with <5 % S). Particles identified in SEM-EDX with processing by IncaFeature.

Table 1

Extraction	Target Phases	Terminology
Na Acetate, pH 4.5, 24 h, 50°C	Carbonate Fe (including siderite and ankerite)	$\text{Fe}_{\text{CARB}}$
Hydroxylamine-HCl, 48 h	Ferrihydrite, lepidocrocite	$\text{Fe}_{\text{OX1}}$
Dithionite, 2 h	Goethite, akaganéite, hematite	$\text{Fe}_{\text{OX2}}$
Oxalate, 6 h	Magnetite	$\text{Fe}_{\text{MAG}}$
Chromous Chloride Distillation	Pyrite Fe	$\text{Fe}_{\text{PY}}$

Table 2

	<b>Al</b> %	<b>Si</b> %	<b>Ti</b> %	<b>Fe</b> %	<b>Mn</b> %	<b>Mg</b> %	<b>Ca</b> %	<b>Na</b> %	<b>K</b> %	<b>P</b> %
<b>BSB.1</b>	2.50	5.57	0.14	1.76	0.01	0.22	5.34	0.09	0.61	0.32
<b>BSB.2</b>	2.50	5.53	0.14	1.76	0.01	0.21	4.63	0.07	0.61	0.34
<b>QVS.1</b>	11.78	25.70	0.58	3.37	0.02	0.45	0.80	0.05	1.76	0.07
<b>QVS.2</b>	11.80 (±0.07)	25.71 (±0.20)	0.58 (±0.00)	3.36 (±0.03)	0.02 (±0.00)	0.43 (±0.01)	0.51 (±0.20)	0.04 (±0.01)	1.70 (±0.01)	0.07 (±0.00)

Table 3

	<b>TOC</b> (%)	<b>TIC</b> (%)	<b>S</b> (%)	<b>PyS</b> (%)	<b>Non-PyS</b> (%)
<b>BSB.1</b>	49.5	4.18	6.71	0.92	5.79
<b>BSB.2</b>	51.15	2.16	6.6	0.59	6.01
<b>QVS.1</b>	2.61	0.37	0.81	1.16	0
<b>QVS.2</b>	2.77 (±0.06)	0.02 (±0.02)	0.62 (±0.02)	0.91 (±0.03)	0

Table 4

	<b>Fe</b> wt%	<b>Fe<sub>Carb</sub></b> wt%	<b>Fe<sub>OX1</sub></b> wt%	<b>Fe<sub>OX2</sub></b> wt%	<b>Fe<sub>Mag</sub></b> wt%	<b>Fe<sub>Py</sub></b> wt%	<b>Fe<sub>PRS</sub></b> wt%	<b>Fe<sub>HR</sub></b> wt%	<b>Fe<sub>HR</sub>/Fe<sub>T</sub></b>	<b>Fe<sub>Py</sub>/Fe<sub>HR</sub></b>
<b>BSB.1</b>	1.76	0.14	0.04	0.02	0	0.8	0.76	1	0.57	0.8
<b>BSB.2</b>	1.76	0.11	0.18	0.26	0.01	0.51	0.69	1.07	0.61	0.54
<b>QVS.1</b>	3.37	0.33	0.6	0.05	0.13	1.01	1.26	2.12	0.63	0.39
<b>QVS.2</b>	3.36 (±0.01)	0.16 (±0.01)	0.54 (±0.02)	0.47 (±0.03)	0.08 (±0.01)	0.79 (±0.02)	1.32 (±0.02)	0	0.61	0.3

**Highlights:**

- A laboratory experiment has stimulated weathering reactions in two different shales
- Total Fe and the redox proxy ( $\text{Fe}_{\text{HR}}/\text{Fe}_{\text{T}}$ ) are unaffected, so reliable in similar shales
- Pyrite oxidation at high pH led to development of Fe oxide rims
- Affected pyrite is observable in SEM and quantifiable with EDX – a new weathering gauge
- Absence of these particles should be confirmed for studies using the  $\text{Fe}_{\text{PY}}/\text{Fe}_{\text{HR}}$  proxy

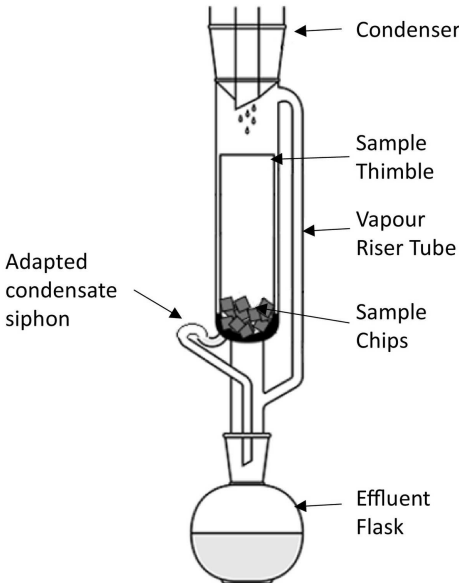
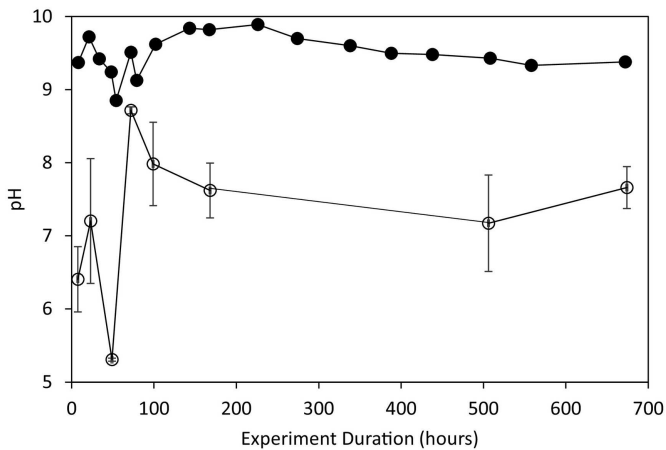


Figure 1

a.



b.

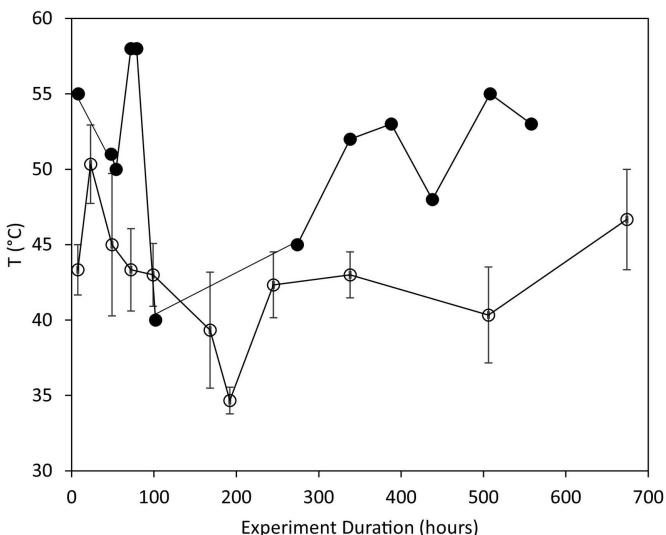


Figure 2

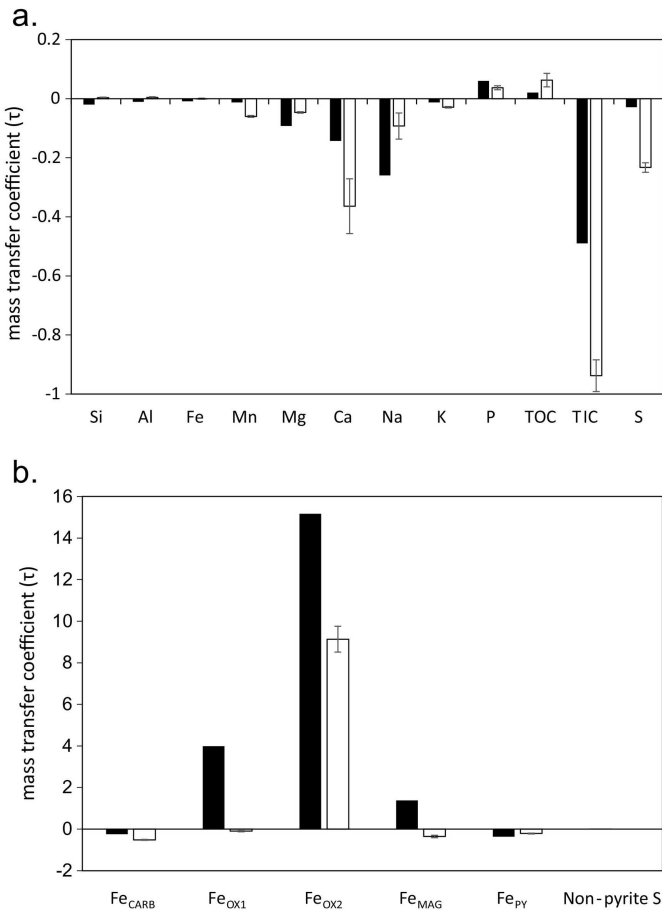


Figure 3

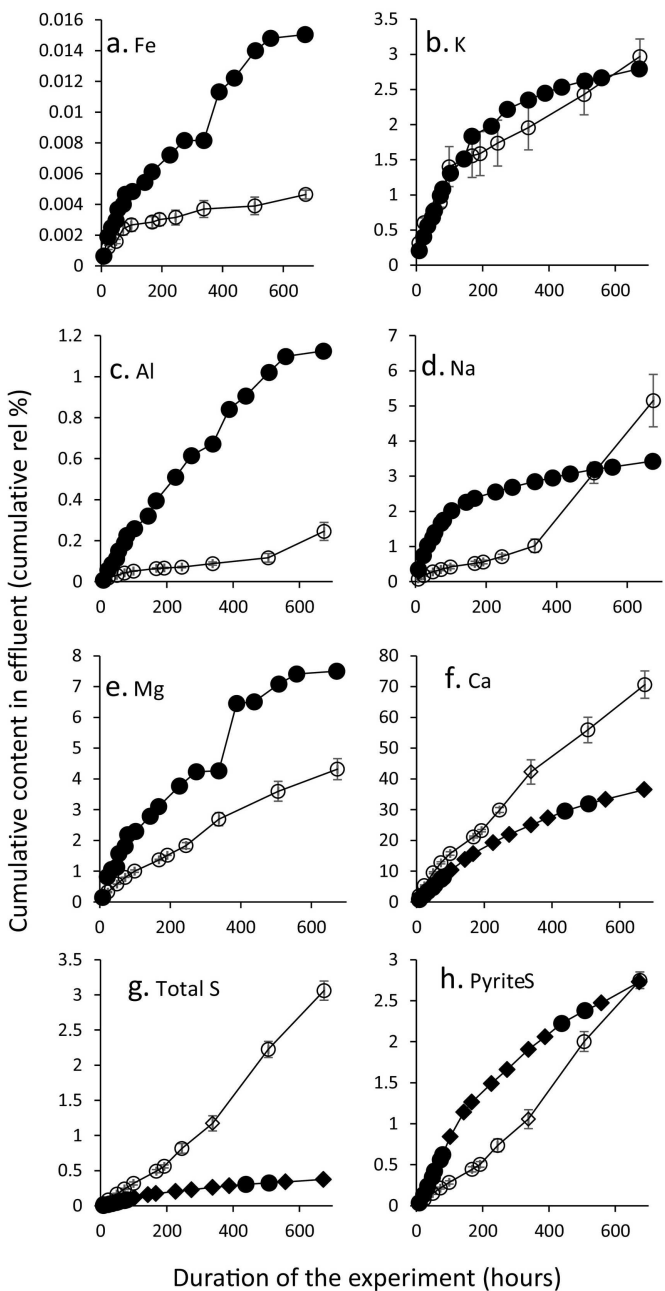


Figure 4

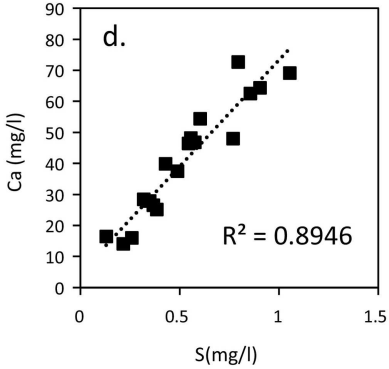
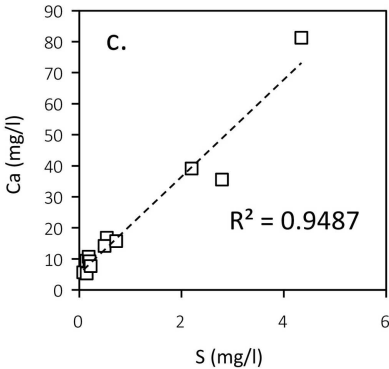
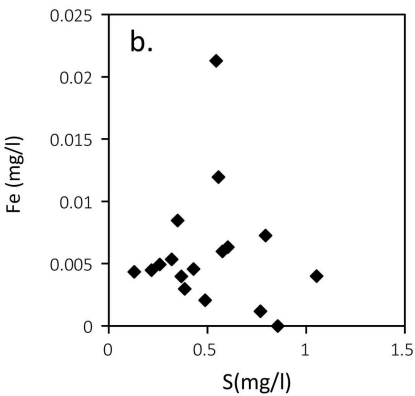
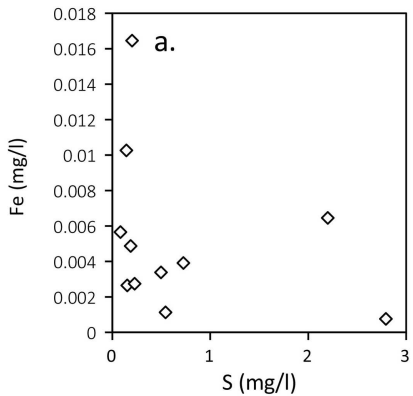
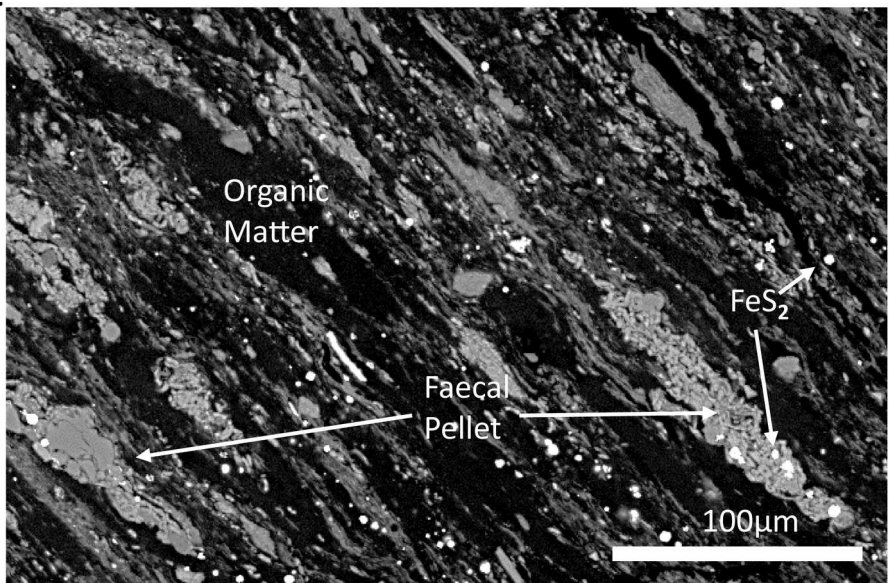
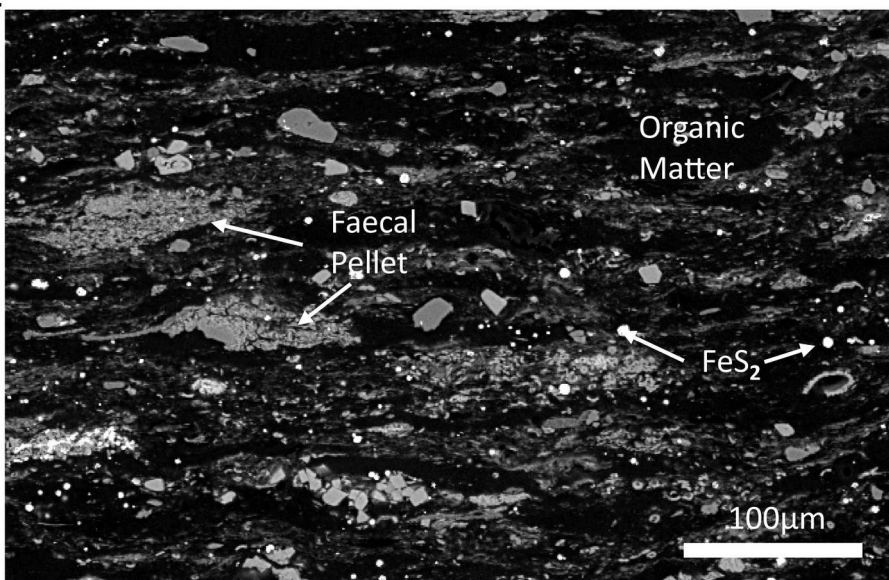


Figure 5

a.



b.



c.

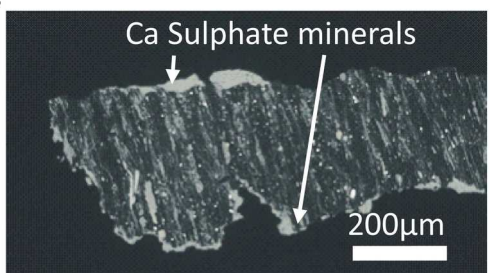
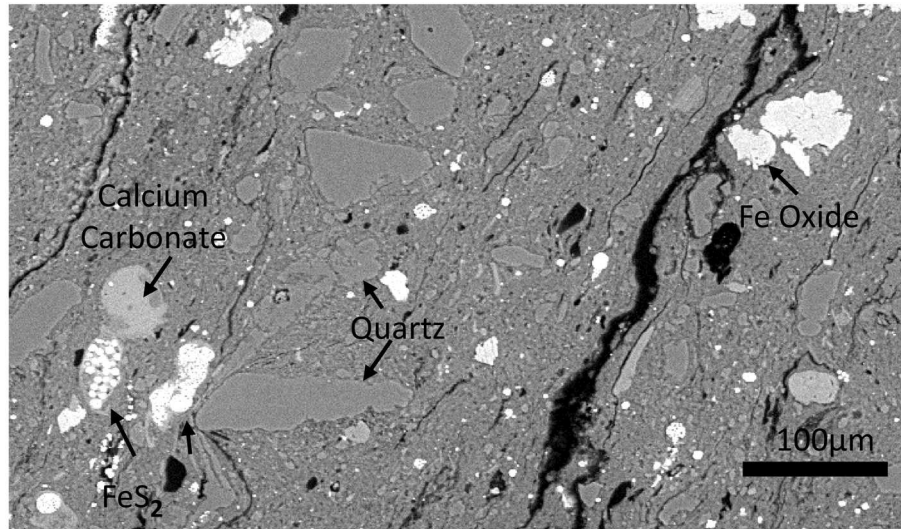


Figure 6

a.



b.

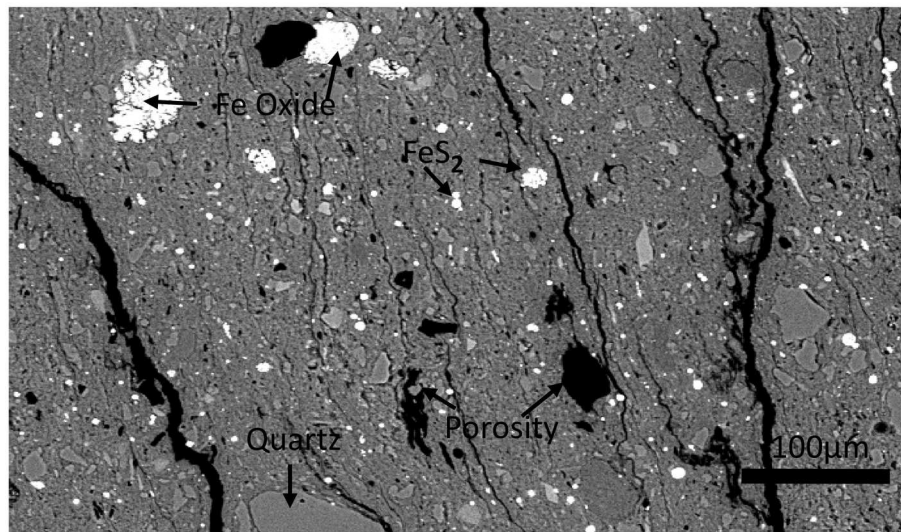
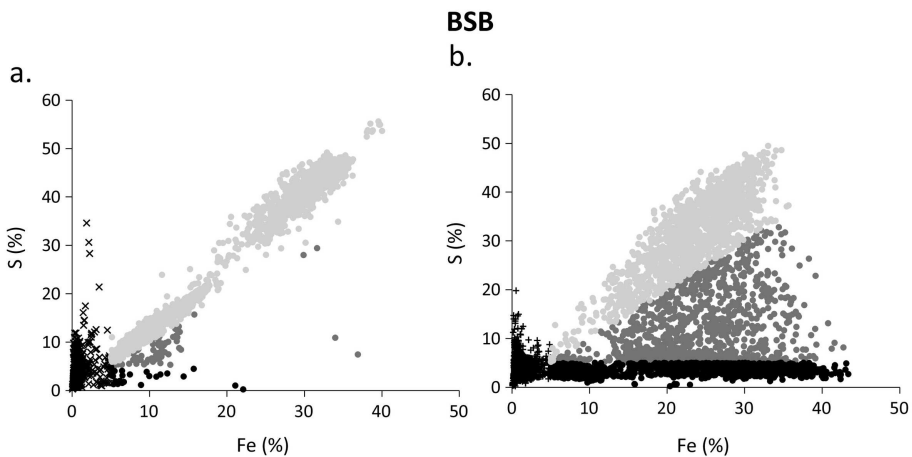


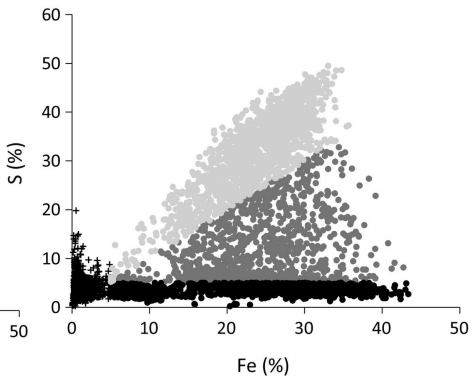
Figure 7

a.

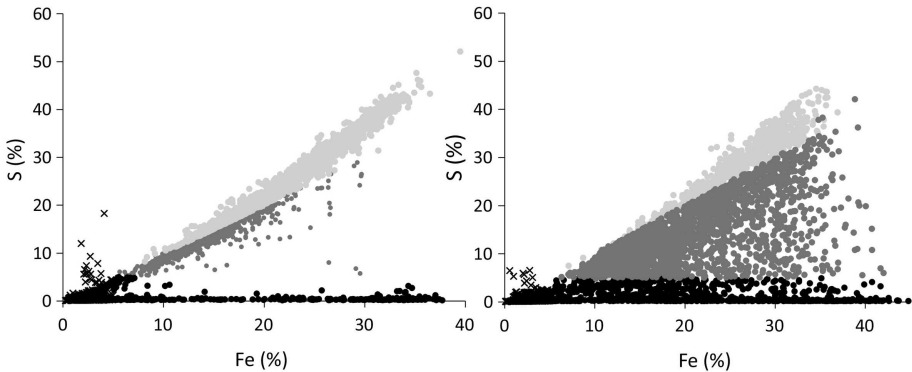


**BSB**

b.



c.



**QVS**

d.

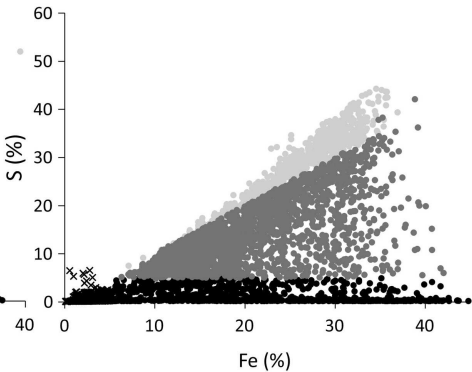
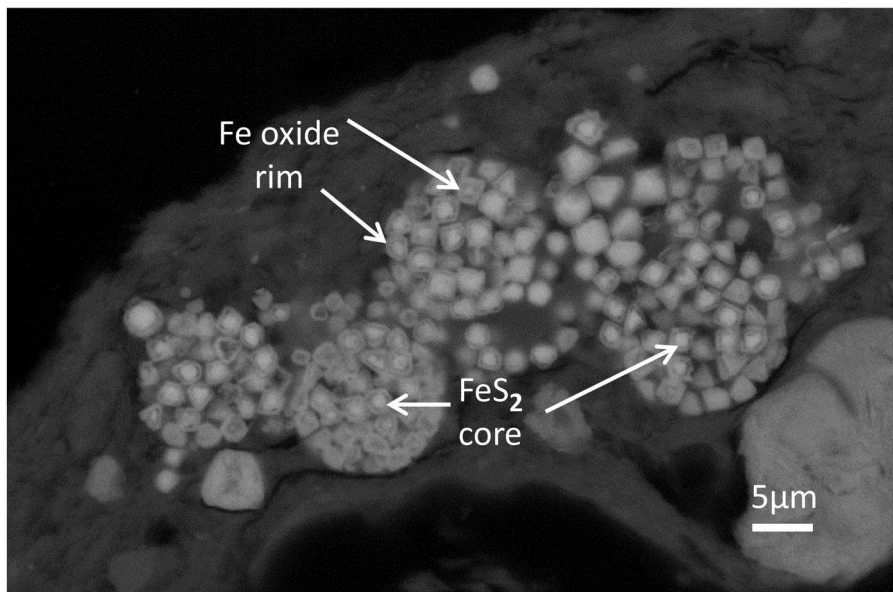
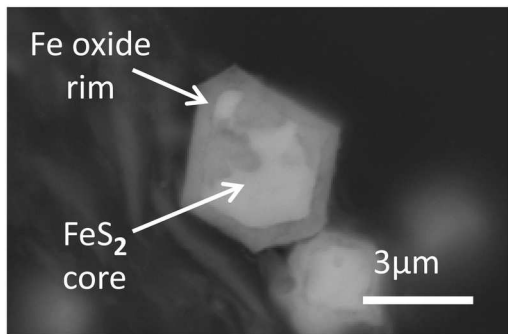


Figure 8

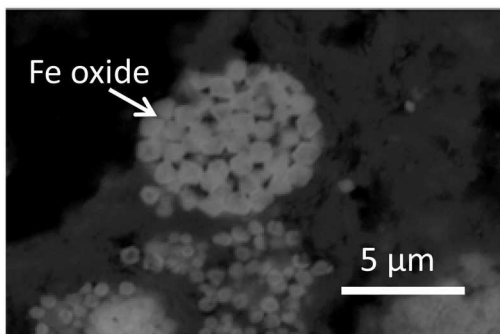
a.



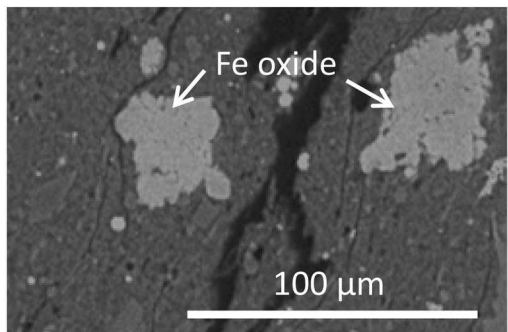
b.



c.



d.



e.

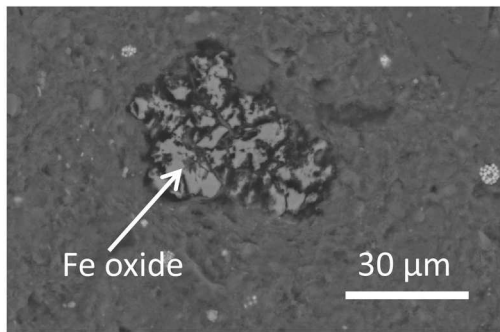


Figure 9

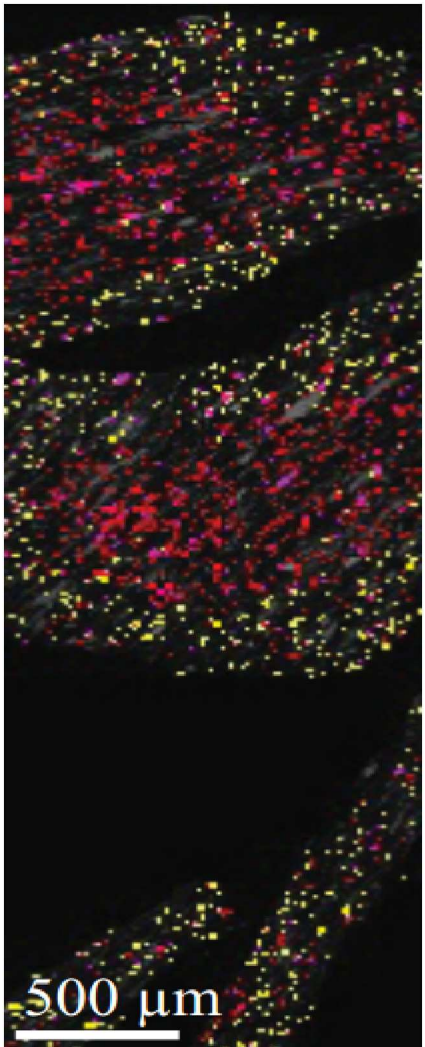


Figure 10

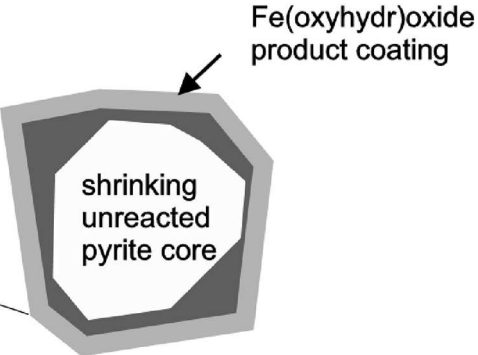
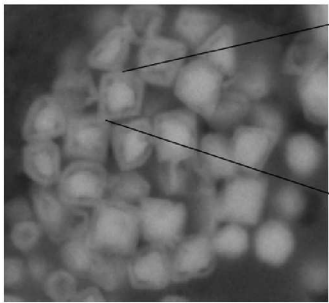


Figure 11